3D Quantum Hall Effect of Fermi Arcs in Topological Semimetals

C. M. Wang,[1,2,3] Hai-Peng Sun,[1,3] Hai-Zhou Lu,[1,3,*] and X. C. Xie[4,5]
[1]Institute for Quantum Science and Engineering and Department of Physics, South University of Science and Technology of China, Shenzhen 518055, China
[2]School of Physics and Electrical Engineering, Anyang Normal University, Anyang 455000, China
[3]Shenzhen Key Laboratory of Quantum Science and Engineering, Shenzhen 518055, China
[4]International Center for Quantum Materials, School of Physics, Peking University, Beijing 100871, China
[5]Collaborative Innovation Center of Quantum Matter, Beijing 100871, China
(Received 13 May 2017; published 28 September 2017)

The quantum Hall effect is usually observed in 2D systems. We show that the Fermi arcs can give rise to a distinctive 3D quantum Hall effect in topological semimetals. Because of the topological constraint, the Fermi arc at a single surface has an open Fermi surface, which cannot host the quantum Hall effect. Via a "wormhole" tunneling assisted by the Weyl nodes, the Fermi arcs at opposite surfaces can form a complete Fermi loop and support the quantum Hall effect. The edge states of the Fermi arcs show a unique 3D distribution, giving an example of $(d-2)$-dimensional boundary states. This is distinctly different from the surface-state quantum Hall effect from a single surface of topological insulator. As the Fermi energy sweeps through the Weyl nodes, the sheet Hall conductivity evolves from the $1/B$ dependence to quantized plateaus at the Weyl nodes. This behavior can be realized by tuning gate voltages in a slab of topological semimetal, such as the TaAs family, Cd_3As_2, or Na_3Bi. This work will be instructive not only for searching transport signatures of the Fermi arcs but also for exploring novel electron gases in other topological phases of matter.

DOI: 10.1103/PhysRevLett.119.136806

Introduction.—The discovery of the quantum Hall effect opens the door to the field of topological phases of matter [1]. In a strong magnetic field, the energy spectrum of a 2D electron gas evolves into Landau levels. The Landau levels deform at the sample edges and cut through the Fermi energy, forming 1D edge states protected by topology [2]. Electrons can flow through the edge states in a dissipationless manner, giving rise to Hall conductance in units of e^2/h that defines the quantum Hall effect. The quantum Hall effect can give transport signatures that distinguish different electron gases, such as the half-integer Hall conductance of the 2D massless Dirac fermions in graphene and topological surface states [1,3–6]. By contrast, in a 3D electron gas, the extra dimension along the magnetic field direction prevents the quantization of the Hall conductance. Therefore, the quantum Hall effect is usually observed in 2D systems.

In this Letter, we show that the quantum Hall effect is possible in a unique 3D system, specifically, in a topological semimetal, because of the Fermi arcs. The topological semimetal is a 3D topological state of matter [7–18], in which energy bands touch at discrete Weyl nodes [Fig. 1(a)]. It is equivalent to a 2D topological insulator for momenta (k_z here) between the Weyl nodes, leading to the topologically protected states located at the surfaces [top and bottom in Fig. 1(c)] parallel to the Weyl node separation direction. The protected states form the Fermi arcs on the Fermi surface [red curves in Figs. 1(a) and 1(b)]. The Fermi arcs have been seen by angle-resolved photoemission spectroscopy [14,16,19–30] and can induce novel quantum oscillations [31,32]. Topological phases of matter usually come with distinctive transports, making the transport signature of the Fermi arcs an intriguing topic [33–37].

There are several issues for the Fermi arcs to exhibit the quantum Hall effect. First, the topological origin requires that the states of Fermi arcs occupy only a region between the Weyl nodes [38] [Fig. 1(b)]. At one surface, the Fermi arcs cannot form a closed Fermi loop needed by Landau levels and the quantum Hall effect. We find that the Fermi arcs from opposite surfaces in a topological semimetal slab [Fig. 1(c)] can complete the needed closed Fermi loop [Fig. 1(d)]. Electrons can tunnel between the Fermi arcs at opposite surfaces via the Weyl nodes [Figs. 1(e)–1(g)]. Second, the quantum Hall effect solely from the Fermi arcs requires the bulk carriers to be depleted by tuning the Fermi energy to the Weyl nodes [39]. Third, we find that the band anisotropy in the bulk Weyl fermions is necessary for the Fermi arcs to form a 2D electron gas. These properties in the quantum Hall effect can provide transport signatures for the Fermi arcs. Compared to the novel quantum oscillations [31,32], the quantum Hall effect of the Fermi arcs contributes a quantum complement to the Fermi-arc-dominant electronic transports. The Weyl semimetals TaAs family [27–30,40–43] and the Dirac semimetals Cd_3As_2 and Na_3Bi have extremely high mobilities [44–48] required by the quantum Hall effect. Low carrier densities [49–51] and gating [49] have also been achieved. We expect the quantum Hall effect of the Fermi arcs in slabs of the TaAs

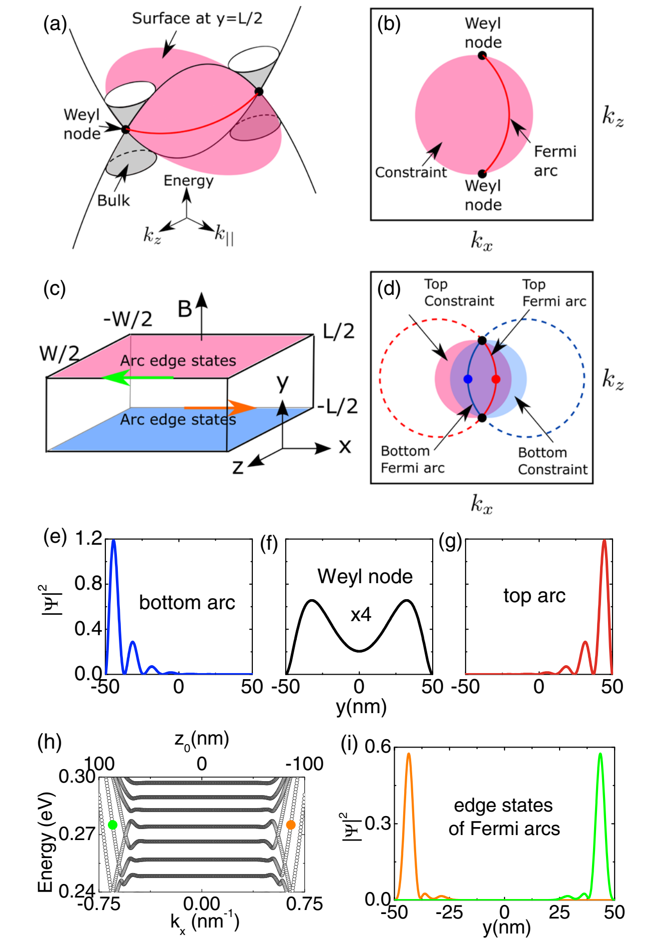

FIG. 1. (a) The energy dispersions for the Fermi arc (at $y = L/2$) and bulk states in a topological Weyl semimetal. $k_{||}$ stands for (k_x, k_y) for the bulk and k_x for the arc, respectively. (b) The Fermi arc at $y = L/2$ and $E_F = E_w$ on the $k_z - k_x$ plane. The shadow defines the "constraint" region where the Fermi arcs can exist. (c) A slab of topological semimetal of thickness L and width W. (d) The Fermi arcs at $E_F = E_w$ (solid) and constraints (shadow) at the $y = L/2$ (red) and $-L/2$ (blue) surfaces of the slab. [(e)–(g)] The wave function distributions at $k_z = 0$ along the y axis, at the blue (bottom arc, $k_x < 0$), black (Weyl nodes), and red (top arc, $k_x > 0$) dots in (d). (h) Landau levels of the Fermi arcs at $B = 5$ T vs the guiding center z_0. (i) The wave function distributions along the y axis for the edge states of the Fermi arcs marked by the green and orange dots in (h). $L = 100$ nm, $W = 200$ nm, and other parameters can be found in Fig. 2.

family, [110] or [1$\bar{1}$0] Cd_3As_2 [52], and [100] or [010] Na_3Bi.

Minimal model.—We will use a minimal model to illustrate the physics for the Fermi-arc quantum Hall effect. To preserve their topological properties, we need to derive the 2D effective model of the Fermi arcs from a 3D model of Weyl semimetal [53–55],

$$H = D_1 k_y^2 + D_2(k_x^2 + k_z^2) + A(k_x\sigma_x + k_y\sigma_y) + M(k_w^2 - k^2)\sigma_z, \quad (1)$$

where $(\sigma_x, \sigma_y, \sigma_z)$ are the Pauli matrices, the wave vector $\mathbf{k} = (k_x, k_y, k_z)$, and D_1, D_2, A, M, and k_w are model parameters. We assume that $|M| > |D_1|$. The energy dispersion of the model is $E_\pm^{\mathbf{k}} = D_1 k_y^2 + D_2(k_x^2 + k_z^2) \pm [M^2(k_w^2 - \mathbf{k}^2)^2 + A^2(k_x^2 + k_y^2)]^{1/2}$, with $\pm$ for the conduction and valence bands, respectively. The model hosts two Weyl nodes at $(0, 0, \pm k_w)$ having energy $E_w = D_2 k_w^2$ [Fig. 1(a)], and carries all of the topological semimetal properties [56]. In contrast to the $k \cdot \sigma$ model, the Fermi arc states can be solved analytically from the model [38].

Open Fermi arc at one surface.—First, we show that the Fermi arc at a single surface of a Weyl semimetal cannot host the quantum Hall effect. We focus on the $y = L/2$ surface. By replacing k_y with $-i\partial_y$ in H and using open-boundary conditions, we can solve the wave function at $k_x = k_z = 0$, and then project H on the wave function to construct the effective model (see the procedure at [38,57,58] and Sec. S1 of [59]) for the Fermi arc,

$$H_{\text{arc}} = D_1 k_w^2 + v k_x + (D_2 - D_1)(k_x^2 + k_z^2), \quad (2)$$

where $v \equiv A\sqrt{M^2 - D_1^2}/M$. If there is no anisotropic D terms, the Fermi arc only disperses linearly with k_x; consequently, the Landau levels cannot be defined. Therefore, the anisotropic D terms are necessary. Moreover, the electron gas of the Fermi arc is distinct from usual 2D electron gases because it is confined within a specific momentum space due to their topological nature [38]. For this model, the Fermi arc at the $y = L/2$ surface is confined in a region defined by the constraint

$$k_x^2 + k_z^2 + 2ak_x < k_w^2, \quad (3)$$

where $a \equiv AD_1/2M\sqrt{M^2 - D_1^2}$. This means that the wave vectors of the Fermi arcs at the $y = L/2$ surface are only allowed within a circle of radius $\sqrt{k_w^2 + a^2}$ centered at $(k_x = -a,\ k_z = 0)$. The Fermi circle of H_{arc} at a given Fermi energy can only partially overlap with the constraint in Eq. (3), forming an "open" Fermi surface, as shown by the red solid curve in Figs. 1(a) and 1(b). Because of the open Fermi surface, electrons cannot undergo complete cyclotron motion in a perpendicular magnetic field. Thus, the 2D electron gas of Fermi arc at a single surface cannot form well-defined Landau levels required by the quantum Hall effect.

Fermi arc loop via "wormhole" tunneling.—In contrast, the Fermi arcs at two opposite surfaces of a slab of Weyl semimetal, with the assistance of the Weyl nodes, can form a closed Fermi loop to support the quantum Hall effect. For a Weyl semimetal slab of thickness L, we consider two opposite surfaces at $y = \pm L/2$ [Fig. 1(c)]. Similar to Eqs. (2) and (3), the model and constraint at the $y = -L/2$ surface are found as $H'_{\text{arc}} = D_1 k_w^2 - v k_x + (D_2 - D_1)(k_x^2 + k_z^2)$ and $k_x^2 + k_z^2 - 2ak_x < k_w^2$, respectively. Figure 1(d) shows the Fermi arcs at $E_F = E_w$ and constraints at the two surfaces. The Fermi arcs at opposite surfaces shift along opposite directions on the k_x axis. The two open Fermi arcs [red and blue curves in Fig. 1(d)] can form a Fermi loop well inside the overlapping constraint regions; thus, all states on this loop are allowed. We numerically calculate the energy spectrum for this slab by using the basis $\varphi_n(y) = \sqrt{2/L}\sin[n\pi(y/L + 1/2)]$ (Sec. S2 of [59]). Figure 2(a) verifies the above picture for the Fermi loop formation. The energy band for the Fermi loop is marked as "I" (arc I). There is another band (marked as "II"), which appears below arc I at $k_x = \pm 0.1\ \mathrm{nm}^{-1}$ but buried in the bulk valence bands. Moreover, the wave function on the Fermi loop can evolve from located at one surface [Figs. 1(e) and 1(g)] to spread out in the y direction [Fig. 1(f)] when moving from the Fermi arcs to the Weyl nodes. Therefore, the Weyl nodes act like "wormholes" that connect the top and bottom

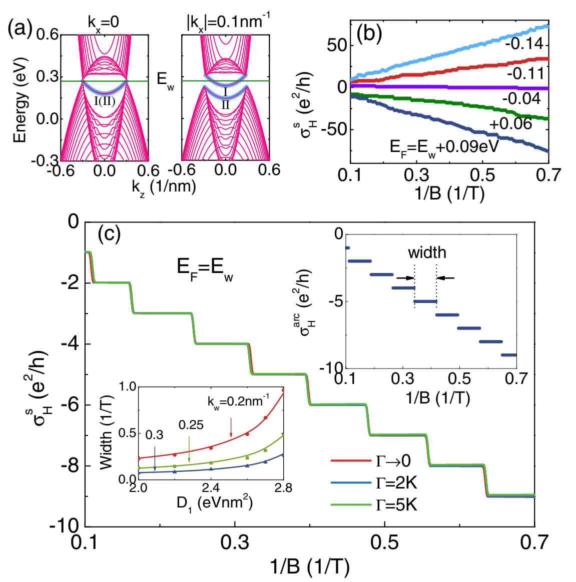

FIG. 2. (a) In a topological semimetal slab, the numerically calculated energy spectrum (pink) for the bulk states and Fermi arcs at $k_x = 0$ (left) and $k_x = \pm 0.1\ \mathrm{nm}^{-1}$ (right). The blue curves are the Fermi arc bands plotted using H_{arc} and H'_{arc}. (b) The sheet Hall conductivity when the Fermi energy E_F crosses the bulk states for $\Gamma \to 0$. Γ is the disorder-induced level broadening. Recent experiments show that gating can tune carriers from n- to p-type in 100-nm-thick devices of topological semimetal [49]. (c) The sheet Hall conductivity σ_{H}^s at $E_F = E_w$, where the Fermi energy crosses only arc I. The right inset shows the analytic Hall conductance $\sigma_{\mathrm{H}}^{\mathrm{arc}}$ in Eq. (5). In the presence of a residual detuning from the Weyl nodes, the bulk states also contribute to σ_{H}^s. Unlike that from the Fermi arcs, the contribution from the bulk states may change with the slab thickness. The left inset shows the width of the Hall plateaus in the clean limit as a function of D_1 for different k_w. The dots and lines are the numerical and analytic results, respectively. The parameters are $M = 5\ \mathrm{eV\,nm}^2$, $A = 0.5\ \mathrm{eV\,nm}$, and $D_2 = 3\ \mathrm{eV\,nm}^2$, $D_1 = 2\ \mathrm{eV\,nm}^2$, $k_w = 0.3\ \mathrm{nm}^{-1}$, and $L = 100$ nm.

surfaces, and an electron can complete the cyclotron motion. Because the Weyl nodes are singularities in both energy and momentum, the wormhole tunneling can be infinite in both time and space, according to the uncertainty principle. In realistic materials, the tunneling distance is limited by the mean free path, which can be comparable to or longer than 100 nm in high-mobility topological semimetals [40–48], even up to 1 μm [32], so the thickness in the calculation is chosen to be 100 nm. The loop formed by the Fermi arcs at opposite surfaces via the Weyl nodes can support a 3D quantum Hall effect. The wormhole effect has been addressed in different situations in topological insulators [60].

The Hall response.—Now we demonstrate that arc I of the Weyl semimetal slab can host the quantum Hall effect. The Hall conductivity can be calculated from the Kubo formula (Sec. S3 of [59]),

$$\sigma_{\mathrm{H}} = \frac{e^2\hbar}{iV_{\mathrm{eff}}}\sum_{\delta,\delta'\neq\delta}\frac{\langle\Psi_\delta|v_x|\Psi_{\delta'}\rangle\langle\Psi_{\delta'}|v_z|\Psi_\delta\rangle[f(E_{\delta'}) - f(E_\delta)]}{(E_\delta - E_{\delta'})(E_\delta - E_{\delta'} + i\Gamma)}. \quad (4)$$

Here $|\Psi_\delta\rangle$ is the eigenstate of energy E_δ for H in a y-direction magnetic field and with open boundaries at $y = \pm L/2$, v_x and v_z are the velocity operators, $f(x)$ is the Fermi distribution, V_{eff} is the volume of the slab or the area of the surfaces that host the Fermi arcs. σ_{H} has a dimension of e^2/h in 2D and of e^2/h over length in 3D. The sheet Hall conductivity for the slab can be defined as $\sigma_{\mathrm{H}}^s = \sigma_{\mathrm{H}}L$. We use the basis $|\phi_\nu(z)\rangle \otimes |\varphi_n(y)\rangle$ to find the eigenenergies for a slab in the y-direction magnetic field, where ϕ_ν are the harmonic oscillator eigenfunctions. Figure 2(b) shows the sheet Hall conductivity for the topological semimetal slab at Fermi energies far away from the Weyl nodes. σ_{H}^s follows the usual $1/B$ dependence. As the Fermi energy is shifted towards the Weyl nodes, the slope becomes smaller, indicating decreasing carrier density. Also, quantized plateaus of σ_{H}^s start to emerge as the Fermi energy approaches the Weyl nodes. When the Fermi energy crosses only arc I [Fig. 2(c)], σ_{H}^s shows well-formed quantized plateaus in units of e^2/h, indicating the quantum Hall effect of the Fermi arcs. Here disorder is included in the Kubo formula via the level broadening Γ. This treatment is capable of giving the quantization in graphene [61], which is massless in 2D. Because of the relation with the Chern number [2], the quantum Hall effect can be theoretically studied in the absence of disorder, as those in topological insulators [62–65]. To verify the numerical result in Fig. 2(c), we also calculate analytically the quantum Hall conductance from arc I (Sec. S4 of [59]), by modeling arc I as an anisotropic parabolic band $H_{\mathrm{arcI}} \approx D_1 k_w^2 + \hbar^2 k_x^2/2m_x + \hbar^2 k_z^2/2m_z$, with m_x and m_z being the effective masses. We can find the quantum Hall conductance of arc I in the clean limit $\Gamma \to 0$ [66,67]

$$\sigma_{\rm H}^{\rm arc}=\frac{e^2}{h}{\rm sgn}(R){\rm sgn}(eB)\left\lfloor\frac{S_{\rm I}/(2\pi)^2}{eB/h}+\frac{1}{2}\right\rfloor, \qquad (5)$$

where $\lfloor\ldots\rfloor$ stands for rounding down, $R=D_2-D_1$ and the area of arc I in momentum space is $S_{\rm I}=2k_w^2(1+v^2/4R^2k_w^2)\arctan(2|R|k_w/|v|)-|v|k_w/|R|$. Figure 2(c) shows a good agreement between the analytic and numerical results on the Hall conductance and width of the plateaus.

Where are the edge states of the Fermi arcs?—Figures 1(h) and 1(i) show that the edge states of the Fermi arcs have a unique 3D spatial distribution. Figure 1(h) shows the energies of the Landau levels in the y-direction field. The energies deform into edge states near $z_0=\pm100$ nm. The green dot in Fig. 1(h) and the green curve in Fig. 1(i) show that the edge state near $z_0=100$ nm mainly distributes near the top surface at $y=50$ nm. By contrast, the edge state near $z_0=-100$ nm mainly distributes near the bottom surface (orange dot and curve). This unique 3D distribution of the edge states of the Fermi arcs can be probed by a combined measurement of in-plane transport and STM. Different from topological insulators [5,6], the Fermi-arc quantum Hall effect requires the collaboration of the two surfaces. Note that a 100-nm slab is still a 3D object. Therefore, the quantum Hall effect at Weyl nodes $E_F=E_w$ and the Fermi energy dependence can serve as transport signatures of the Fermi arcs. The above picture for the Fermi-arc quantum Hall effect can work for Weyl semimetals [27–30,39–43].

Topological Dirac semimetals.—Because of time-reversal symmetry, a single surface of the Dirac semimetal, such as Cd_3As_2 and Na_3Bi, can support a complete Fermi loop required by the quantum Hall effect. The same-surface Fermi arc loop is not that robust and may get deformed [68], and thus may show different characteristics (such as positions and widths of the Hall plateaus) compared to the two-surface Fermi arc loop. The spectrum and Fermi-arc Hall effect in Dirac semimetals can be studied (Secs. S5 and S6 of [59]) by using the Hamiltonian [14,16,69]

$$H=\epsilon_0(\boldsymbol{k})+\begin{bmatrix} M(\boldsymbol{k}) & Ak_+ & 0 & 0\\ Ak_- & -M(\boldsymbol{k}) & 0 & 0\\ 0 & 0 & M(\boldsymbol{k}) & -Ak_-\\ 0 & 0 & -Ak_+ & -M(\boldsymbol{k})\end{bmatrix} +\frac{\mu_B}{2}(\boldsymbol{\sigma}\cdot\boldsymbol{B})\otimes\begin{bmatrix} g_s & 0\\ 0 & g_p\end{bmatrix}, \qquad (6)$$

where g_s and g_p are the g factors for the s and p bands [69], $k_\pm=k_x\pm ik_y$, $\epsilon_0(\boldsymbol{k})=C_0+C_1k_z^2+C_2(k_x^2+k_y^2)$, and $M(\boldsymbol{k})=M_0+M_1k_z^2+M_2(k_x^2+k_y^2)$. The x, y, and z axes

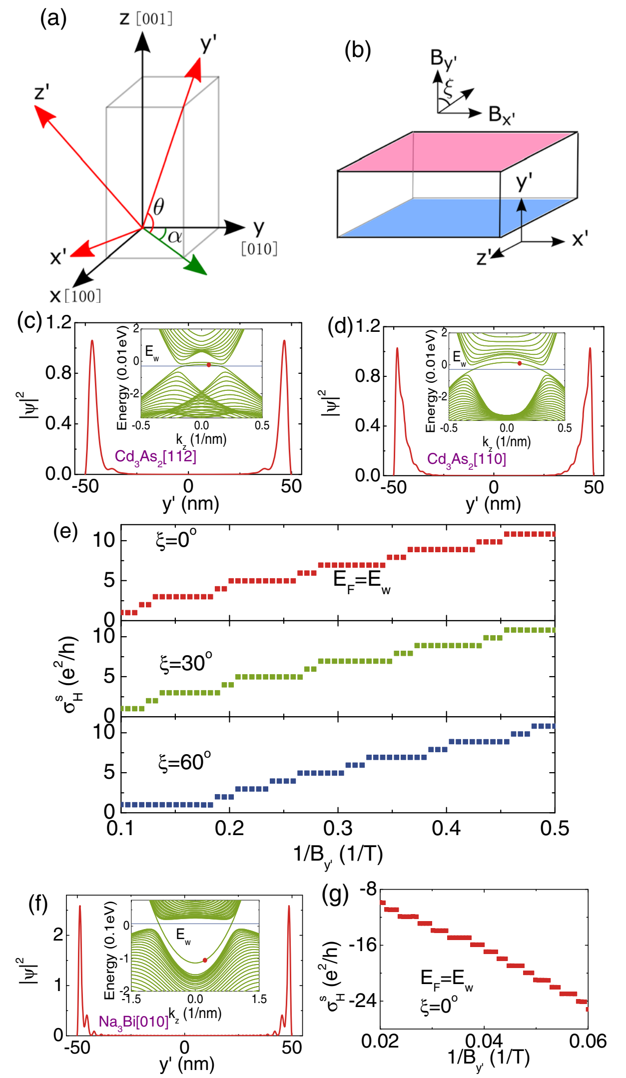

FIG. 3. (a) The crystallographic directions and coordinates system in the model of Dirac semimetal Eq. (6). Slabs grown along the [112] and [110] directions corresponds to $(\alpha,\theta)=(-\pi/4,\tan^{-1}\sqrt{2})$ and $(-\pi/4,0)$, respectively. (b) y' is the slab growth direction. The Hall conductance is defined in the $x'-z'$ plane. The magnetic field can be rotated from the y' to the x' direction by the angle ξ. [(c),(d),(f)] For a slab of 100 nm, the energy spectrum at $k_x=0.01$ nm^{-1} and the wave function distribution along the y' direction for the states marked by the red points. (e) The sheet Hall conductivity at the Dirac node $E_w=C_0-C_1M_0/M_1$ for the Cd_3As_2 [110] slab at different ξ. (g) The same as (e) but for the [010] Na_3Bi slab. The parameters for Cd_3As_2 are $C_0=-0.0145$ eV, $C_1=10.59$ eV Å^2, $C_2=11.5$ eV Å^2, $M_0=0.0205$ eV, $M_1=-18.77$ eV Å^2, $M_2=-13.5$ eV Å^2, $A=0.889$ eV Å [70], $g_s=18.6$, and $g_p=2$ [69]. The parameters for Na_3Bi are $C_0=-0.06382$ eV, $C_1=8.7536$ eV Å^2, $C_2=-8.4008$ eV Å^2, $M_0=0.08686$ eV, $M_1=-10.6424$ eV Å^2, $M_2=-10.361$ eV Å^2, $A=2.4598$ eV Å [70] $g_s=20$, and $g_p=20$ [48]. $\Gamma=1$ K in panels (e) and (g).

in the Hamiltonian are defined along the [100], [010], and [001] crystallographic directions, respectively. The samples of Cd_3As_2 are usually cleaved or grown along [112] or [110] directions, which can be defined as the new y' axis for convenience, as shown in Fig. 3(a). For the [112] slab, the parameters [70] yield that the Fermi arc bands are close to the bulk subbands [Fig. 3(c)], implying that the quantum Hall effect may exhibit a fourfold degeneracy. For the [110] slab, the quantum Hall effect may come from pure Fermi arc states [Fig. 3(d)]. Figure 3(e) shows that for the [110] Cd_3As_2 slab the odd plateaus are wider than the even plateaus, because the g factor is large. This feature is robust when rotating the magnetic field. The Na_3Bi samples cleaved along the [010] direction [22] can be used to probe the quantum Hall effect of the Fermi arcs [Figs. 3(f) and 3(g)]. The C and M terms in Eq. (6) secure the 2D Fermi arc on the (010) surface.

We thank helpful discussions with Faxian Xiu, Wang Yao, Hongming Weng, Xi Dai, Dapeng Yu, Yusheng Zhao, Wenqing Zhang, Jiaqing He, and Lang Chen. This work was supported by National Basic Research Program of China (NBRPC) (Grant No. 2015CB921102), Guangdong Innovative and Entrepreneurial Research Team Program (Grant No. 2016ZT06D348), the National Key R & D Program (Grant No. 2016YFA0301700), the National Natural Science Foundation of China (Grants No. 11534001, No. 11474005, and No. 11574127), and the Science, Technology and Innovation Commission of Shenzhen Municipality (Grant No. ZDSYS20170303165926217).

*Corresponding author.
luhz@sustc.edu.cn

[1] K. v. Klitzing, G. Dorda, and M. Pepper, New Method for High-Accuracy Determination of the Fine-Structure Constant Based on Quantized Hall Resistance, Phys. Rev. Lett. **45**, 494 (1980).
[2] D. J. Thouless, M. Kohmoto, M. P. Nightingale, and M. den Nijs, Quantized Hall Conductance in a Two-Dimensional Periodic Potential, Phys. Rev. Lett. **49**, 405 (1982).
[3] K. S. Novoselov, A. K. Geim, S. V. Morozov, D. Jiang, M. I. Katsnelson, I. V. Grigorieva, S. V. Dubonos, and A. A. Firsov, Two-dimensional gas of massless Dirac fermions in graphene, Nature (London) **438**, 197 (2005).
[4] Y. Zhang, Y.-W. Tan, H. L. Stormer, and P. Kim, Experimental observation of the quantum Hall effect and Berry's phase in graphene, Nature (London) **438**, 201 (2005).
[5] Y. Xu, I. Miotkowski, C. Liu, J. Tian, H. Nam, N. Alidoust, J. Hu, C.-K. Shih, M. Z. Hasan, and Y. P. Chen, Observation of topological surface state quantum Hall effect in an intrinsic three-dimensional topological insulator, Nat. Phys. **10**, 956 (2014).
[6] R. Yoshimi, K. Yasuda, A. Tsukazaki, K. S. Takahashi, N. Nagaosa, M. Kawasaki, and Y. Tokura, Quantum Hall states stabilized in semi-magnetic bilayers of topological insulators, Nat. Commun. **6**, 8530 (2015).
[7] X. Wan, A. M. Turner, A. Vishwanath, and S. Y. Savrasov, Topological semimetal and Fermi-arc surface states in the electronic structure of pyrochlore iridates, Phys. Rev. B **83**, 205101 (2011).
[8] K. Y. Yang, Y. M. Lu, and Y. Ran, Quantum Hall effects in a Weyl semimetal: Possible application in pyrochlore iridates, Phys. Rev. B **84**, 075129 (2011).
[9] A. A. Burkov and L. Balents, Weyl Semimetal in a Topological Insulator Multilayer, Phys. Rev. Lett. **107**, 127205 (2011).
[10] G. Xu, H. M. Weng, Z. J. Wang, X. Dai, and Z. Fang, Chern Semimetal and the Quantized Anomalous Hall Effect in $HgCr_2Se_4$, Phys. Rev. Lett. **107**, 186806 (2011).
[11] P. Delplace, J. Li, and D. Carpentier, Topological Weyl semimetal from a lattice model, Europhys. Lett. **97**, 67004 (2012).
[12] J.-H. Jiang, Tunable topological Weyl semimetal from simple-cubic lattices with staggered fluxes, Phys. Rev. A **85**, 033640 (2012).
[13] S. M. Young, S. Zaheer, J. C. Y. Teo, C. L. Kane, E. J. Mele, and A. M. Rappe, Dirac Semimetal in Three Dimensions, Phys. Rev. Lett. **108**, 140405 (2012).
[14] Z. Wang, Y. Sun, X. Q. Chen, C. Franchini, G. Xu, H. Weng, X. Dai, and Z. Fang, Dirac semimetal and topological phase transitions in A_3Bi (A = Na, K, Rb), Phys. Rev. B **85**, 195320 (2012).
[15] B. Singh, A. Sharma, H. Lin, M. Z. Hasan, R. Prasad, and A. Bansil, Topological electronic structure and Weyl semimetal in the $TlBiSe_2$ class of semiconductors, Phys. Rev. B **86**, 115208 (2012).
[16] Z. Wang, H. Weng, Q. Wu, X. Dai, and Z. Fang, Three-dimensional Dirac semimetal and quantum transport in Cd_3As_2, Phys. Rev. B **88**, 125427 (2013).
[17] J. Liu and D. Vanderbilt, Weyl semimetals from noncentrosymmetric topological insulators, Phys. Rev. B **90**, 155316 (2014).
[18] D. Bulmash, C.-X. Liu, and X.-L. Qi, Prediction of a Weyl semimetal in HgCdMnTe, Phys. Rev. B **89**, 081106 (2014).
[19] M. Brahlek, N. Bansal, N. Koirala, S. Y. Xu, M. Neupane, C. Liu, M. Z. Hasan, and S. Oh, Topological-Metal to Band-Insulator Transition in $(Bi_{1-x}In_x)_2Se_3$ Thin Films, Phys. Rev. Lett. **109**, 186403 (2012).
[20] L. Wu, M. Brahlek, R. Valdes Aguilar, A. V. Stier, C. M. Morris, Y. Lubashevsky, L. S. Bilbro, N. Bansal, S. Oh, and N. P. Armitage, A sudden collapse in the transport lifetime across the topological phase transition in $(Bi_{1-x}In_x)_2Se_3$, Nat. Phys. **9**, 410 (2013).
[21] Z. K. Liu *et al.*, Discovery of a three-dimensional topological Dirac semimetal, Na_3Bi, Science **343**, 864 (2014).
[22] S. Y. Xu *et al.*, Observation of Fermi arc surface states in a topological metal, Science **347**, 294 (2015).
[23] Z. K. Liu *et al.*, A stable three-dimensional topological Dirac semimetal Cd_3As_2, Nat. Mater. **13**, 677 (2014).
[24] M. Neupane *et al.*, Observation of a three-dimensional topological Dirac semimetal phase in high-mobility Cd_3As_2, Nat. Commun. **5**, 3786 (2014).
[25] H. Yi *et al.*, Evidence of topological surface state in three-dimensional Dirac semimetal Cd_3As_2, Sci. Rep. **4**, 6106 (2014).

[26] S. Borisenko, Q. Gibson, D. Evtushinsky, V. Zabolotnyy, B. Büchner, and R. J. Cava, Experimental Realization of a Three-Dimensional Dirac Semimetal, Phys. Rev. Lett. **113**, 027603 (2014).

[27] H. M. Weng, C. Fang, Z. Fang, B. A. Bernevig, and X. Dai, Weyl Semimetal Phase in Noncentrosymmetric Transition-Metal Monophosphides, Phys. Rev. X **5**, 011029 (2015).

[28] S. M. Huang *et al.*, A Weyl fermion semimetal with surface Fermi arcs in the transition metal monopnictide TaAs class, Nat. Commun. **6**, 7373 (2015).

[29] B. Q. Lv *et al.*, Experimental Discovery of Weyl Semimetal TaAs, Phys. Rev. X **5**, 031013 (2015).

[30] S. Y. Xu *et al.*, Discovery of a Weyl fermion semimetal and topological Fermi arcs, Science **349**, 613 (2015).

[31] A. C. Potter, I. Kimchi, and A. Vishwanath, Quantum oscillations from surface Fermi arcs in Weyl and Dirac semimetals, Nat. Commun. **5**, 5161 (2014).

[32] P. J. W. Moll, N. L. Nair, T. Helm, A. C. Potter, I. Kimchi, A. Vishwanath, and J. G. Analytis, Transport evidence for Fermi-arc-mediated chirality transfer in the Dirac semimetal Cd_3As_2, Nature (London) **535**, 266 (2016).

[33] P. Hosur, Friedel oscillations due to Fermi arcs in Weyl semimetals, Phys. Rev. B **86**, 195102 (2012).

[34] Y. Baum, E. Berg, S. A. Parameswaran, and A. Stern, Current at a Distance and Resonant Transparency in Weyl Semimetals, Phys. Rev. X **5**, 041046 (2015).

[35] E. V. Gorbar, V. A. Miransky, I. A. Shovkovy, and P. O. Sukhachov, Origin of dissipative Fermi arc transport in Weyl semimetals, Phys. Rev. B **93**, 235127 (2016).

[36] Y. Ominato and M. Koshino, Magnetotransport in Weyl semimetals in the quantum limit: Role of topological surface states, Phys. Rev. B **93**, 245304 (2016).

[37] T. M. McCormick, S. J. Watzman, J. P. Heremans, and N. Trivedi, Fermi arc mediated entropy transport in topological semimetals, arXiv:1703.04606.

[38] S.-B. Zhang, H.-Z. Lu, and S.-Q. Shen, Linear magnetoconductivity in an intrinsic topological Weyl semimetal, New J. Phys. **18**, 053039 (2016).

[39] J. Ruan, S.-K. Jian, H. Yao, H. Zhang, S.-C. Zhang, and D. Xing, Symmetry-protected ideal Weyl semimetal in HgTe-class materials, Nat. Commun. **7**, 11136 (2016).

[40] X. C. Huang *et al.*, Observation of the Chiral-Anomaly-Induced Negative Magnetoresistance in 3D Weyl Semimetal TaAs, Phys. Rev. X **5**, 031023 (2015).

[41] L. X. Yang *et al.*, Weyl semimetal phase in the non-centrosymmetric compound TaAs, Nat. Phys. **11**, 728 (2015).

[42] C. Shekhar *et al.*, Extremely large magnetoresistance and ultrahigh mobility in the topological Weyl semimetal NbP, Nat. Phys. **11**, 645 (2015).

[43] C. L. Zhang *et al.*, Signatures of the Adler-Bell-Jackiw chiral anomaly in a Weyl Fermion semimetal, Nat. Commun. **7**, 10735 (2016).

[44] L. P. He, X. C. Hong, J. K. Dong, J. Pan, Z. Zhang, J. Zhang, and S. Y. Li, Quantum Transport Evidence for the Three-Dimensional Dirac Semimetal Phase in Cd_3As_2, Phys. Rev. Lett. **113**, 246402 (2014).

[45] T. Liang, Q. Gibson, M. N. Ali, M. H. Liu, R. J. Cava, and N. P. Ong, Ultrahigh mobility and giant magnetoresistance in the Dirac semimetal Cd_3As_2, Nat. Mater. **14**, 280 (2015).

[46] Y. F. Zhao *et al.*, Anisotropic Fermi Surface and Quantum Limit Transport in High Mobility Three-Dimensional Dirac Semimetal Cd_3As_2, Phys. Rev. X **5**, 031037 (2015).

[47] A. Narayanan *et al.*, Linear Magnetoresistance Caused By Mobility Fluctuations in n-Doped Cd_3As_2, Phys. Rev. Lett. **114**, 117201 (2015).

[48] J. Xiong, S. K. Kushwaha, T. Liang, J. W. Krizan, M. Hirschberger, W. Wang, R. J. Cava, and N. P. Ong, Evidence for the chiral anomaly in the Dirac semimetal Na_3Bi, Science **350**, 413 (2015).

[49] C. Z. Li, L. X. Wang, H. W. Liu, J. Wang, Z. M. Liao, and D. P. Yu, Giant negative magnetoresistance induced by the chiral anomaly in individual Cd_3As_2 nanowires, Nat. Commun. **6**, 10137 (2015).

[50] H. Li, H. T. He, H. Z. Lu, H. C. Zhang, H. C. Liu, R. Ma, Z. Y. Fan, S. Q. Shen, and J. N. Wang, Negative magnetoresistance in Dirac semimetal Cd_3As_2, Nat. Commun. **7**, 10301 (2016).

[51] C. Zhang *et al.*, Room-temperature chiral charge pumping in Dirac semimetals, Nat. Commun. **8**, 13741 (2017).

[52] M. Uchida *et al.*, APS March Meeting (2017), Abstract No. A44.00005 https://meetings.aps.org/Meeting/MAR17/Session/A44.5.

[53] S.-Q. Shen, *Topological Insulators* (Springer-Verlag, Berlin Heidelberg, 2012).

[54] R. Okugawa and S. Murakami, Dispersion of Fermi arcs in Weyl semimetals and their evolutions to dirac cones, Phys. Rev. B **89**, 235315 (2014).

[55] H. Z. Lu, S. B. Zhang, and S. Q. Shen, High-field magnetoconductivity of topological semimetals with short-range potential, Phys. Rev. B **92**, 045203 (2015).

[56] H.-Z. Lu and S.-Q. Shen, Quantum transport in topological semimetals under magnetic fields, Front. Phys. **12**, 127201 (2017).

[57] H. Z. Lu, W. Y. Shan, W. Yao, Q. Niu, and S. Q. Shen, Massive Dirac fermions and spin physics in an ultrathin film of topological insulator, Phys. Rev. B **81**, 115407 (2010).

[58] W.-Y. Shan, H.-Z. Lu, and S.-Q. Shen, Effective continuous model for surface states and thin films of three-dimensional topological insulators, New J. Phys. **12**, 043048 (2010).

[59] See Supplemental Material at http://link.aps.org/supplemental/10.1103/PhysRevLett.119.136806 for detailed calculations.

[60] G. Rosenberg, H.-M. Guo, and M. Franz, Wormhole effect in a strong topological insulator, Phys. Rev. B **82**, 041104 (2010).

[61] V. P. Gusynin and S. G. Sharapov, Unconventional Integer Quantum Hall Effect in Graphene, Phys. Rev. Lett. **95**, 146801 (2005).

[62] A. A. Zyuzin and A. A. Burkov, Thin topological insulator film in a perpendicular magnetic field, Phys. Rev. B **83**, 195413 (2011).

[63] S. B. Zhang, Y. Y. Zhang, and S. Q. Shen, Robustness of quantum spin Hall effect in an external magnetic field, Phys. Rev. B **90**, 115305 (2014).

[64] S. B. Zhang, H. Z. Lu, and S. Q. Shen, Edge states and integer quantum Hall effect in topological insulator thin films, Sci. Rep. **5**, 13277 (2015).

[65] A. Pertsova, C. M. Canali, and A. H. MacDonald, Quantum Hall edge states in topological insulator nanoribbons, Phys. Rev. B **94**, 121409 (2016).
[66] J. K. Jain, *Composite Fermions* (Cambridge University Press, Cambridge, England, 2007).
[67] R. B. Laughlin, Quantized Hall conductivity in two dimensions, Phys. Rev. B **23**, 5632 (1981).
[68] M. Kargarian, M. Randeria, and Y.-M. Lu, Are the surface Fermi arcs in Dirac semimetals topologically protected?, Proc. Natl. Acad. Sci. U.S.A. **113**, 8648 (2016).
[69] S. Jeon, B. B. Zhou, A. Gyenis, B. E. Feldman, I. Kimchi, A. C. Potter, Q. D. Gibson, R. J. Cava, A. Vishwanath, and A. Yazdani, Landau quantization and quasiparticle interference in the three-dimensional Dirac semimetal Cd_3As_2, Nat. Mater. **13**, 851 (2014).
[70] J. Cano, B. Bradlyn, Z. Wang, M. Hirschberger, N. P. Ong, and B. A. Bernevig, Chiral anomaly factory: Creating Weyl fermions with a magnetic field, Phys. Rev. B **95**, 161306 (2017).